Braz J Phys
DOI 10.1007/s13538-016-0409-4

SOCIEDADE BRASILEIRA DE FÍSICA

CONDENSED MATTER

Whole-Pattern Fitting and Positron Annihilation Studies of Magnetic PVA/α-Fe_2O_3 Nanocomposites

K. S. Prashanth[1] · S. S. Mahesh[2] · M. B. Nanda Prakash[3] · S. Ningaraju[3] · H. B. Ravikumar[3] · R. Somashekar[3] · B. M. Nagabhushana[4]

Received: 12 January 2016

Abstract A low-temperature solution combustion method was used to synthesize α-Fe_2O_3 nanoparticles. Magnetic polyvinyl alcohol (PVA)/α-Fe_2O_3/NaCl nanocomposites were prepared by solvent cast method. The Fourier transform infrared (FTIR) spectroscopy and scanning electron microscopy (SEM) results are in confirmation with X-ray diffraction (XRD) results indicating the formation of nanocomposites. The microcrystalline parameters, crystallite size (<*N*>), lattice strain (*g* in %), stacking faults (α_d), and twin faults (β) of prepared polymer nanocomposites were evaluated by whole-pattern fitting technique. The refinement was carried out using the computed microstructural parameters in which the twin faults and stacking faults did not vary much and statistical deviation was less than 5 %. Positron annihilation lifetime spectroscopy (PALS) was used for microstructural characterization. PALS results show that the ortho-positronium (o-Ps) lifetime (τ_3) increases gradually as a function of nanoparticle concentration and about 219 ps increase observed from1.50 to1.71 ns at 3 wt%. This indicates the increase of free volume hole size (V_f) from 54.47 to 72.18 Å^3. The o-Ps intensities (I_3) decrease indicating the inhibition of o-Ps formation upon incorporation of nanoparticles into PVA. The increase in I_2 values suggests the increased annihilation at the interface region. Positron lifetime parameters, viz., o-Ps lifetime, and its intensities indicate the effect of quenching and inhibition upon incorporation of metal oxide nanoparticles and inorganic salt into PVA.

Keywords Microstructural parameters · Line profile analysis · PALS · Solution combustion method · Magnetic nanocomposites

1 Introduction

In synthesizing polymer nanocomposites, a demanding task is the inadequacy of the interaction between the polymer matrix and the nanofillers. The lack of methodical investigation of the effect of nanostructures on the pristine polymers opens up plethora of opportunities in controlling the quality and to tailor-made the properties of the synthesized polymer nanocomposites. The nanoparticles can bring out phenomenal changes in physical, mechanical, rheological, chemical, and biomedical [1–3] properties of host polymer. On the other hand, the nanoparticles could also have undesirable effects [4, 5] on the polymer matrix. Recently, magnetic metal oxides and their composites are of specific interest for their invigorating applications in the areas of drug delivery [6], memory devices [7], stem cell labeling [8], biosensors [9], bactericidal [10], and EMI shielding [11]. In polymeric composites, the polymer plays the role of reducing the aggregation of particles and imposes the upper limit on the size of inorganic particles. As microstructural defects in polymer nanocomposites may significantly alter the properties of this new class of functional materials, microstructural characterization is vividly important. In this study, a simple and less expensive solution

✉ S. S. Mahesh
maheshphysics1976@gmail.com

[1] Department of Physics, New Horizon college of Engineering, Bangalore, Karnataka 560103, India

[2] Department of Physics, Acharya Institute of Technology, Bangalore, Karnataka 560 107, India

[3] RIE, University of Mysore, Manasagangotri, Mysore, Karnataka 570006, India

[4] Department of Chemistry, M S Ramiah Institute of Technology, Bangalore, Karnataka 560064, India

Published online: 08 March 2016

combustion synthesis method was used to synthesize iron oxide nanoparticles. The ecofriendly, biocompatible material, polyvinyl alcohol (PVA), was chosen as the host polymer. To prevent the nanoparticle agglomeration, environmentally mild inorganic salt sodium chloride was used as the spacer.

In recent years, positron lifetime technique has emerged as a unique and potent probe for directly characterizing the free volume cavities and their concentration in the amorphous region of the polymers in terms of positron lifetime of the injected positrons [12]. Free volume holes provide pathways for thermal motion of the chain segments. The varieties of structural changes like first-order phase transition and second-order phase transitions like glass transition and relaxation processes in polymers and polymer composites are well described by considering the free volume as an internal material parameter [13].

A brief description of the positron annihilation lifetime spectroscopy is given below: When an energetic positron from a radioactive source enters a condensed medium like polymer, it thermalizes quickly by losing all its energy in a very short time, and then annihilates with an electron of the medium. Annihilation usually takes place from different positron states, viz., free annihilation, or from a localized state (trapped state) or from a bound state called positronium (Ps). Ps can exist in two spin states, a para-positronium (p-Ps, spin antiparallel), which annihilates with a lifetime of 0.125 ns, and ortho-positronium (o-Ps, spin parallel), which annihilates with a lifetime of 140 ns in free space. In condensed matter, the o-Ps annihilates predominantly through a fast channel with an electron of the surrounding medium possessing an opposite spin; a process called pick-off annihilation and the o-Ps lifetime get reduced to a few nanoseconds. Each of these annihilation processes has a characteristic lifetime. In polymers, the o-Ps lifetime is an important parameter since positronium is trapped and annihilated in free volume sites, and hence it determines the size of free volume holes in the polymer matrix [13].

In establishing structure–property relationship, identification of the phases forms the first step in structure characterization and evaluation of microstructural parameters is the second step. Hence, microstructural defect characterization in polymer nanocomposites is an integral part of polymer nanotechnological applications. In this paper, whole-pattern fitting technique which is an extension of single-order method developed indigenously by our team has been used for computation. This method has the potential to subdue the dense overlap of reflections and the averaging effect for the coherent errors arising from distribution of nanoparticles in the polymer matrix. Moreover, the defect characterization in polymer nanocomposites using X-ray line profile analysis and PALS is absent in the literature. In addition to this, in our earlier studies, only the o-Ps intensity (I_3) variation was reported, but in this study, variation of o-Ps intensities (I_2) is also investigated which is not reported elsewhere.

2 Experimental

2.1 Materials

PVA of molecular weight ~60 kDa was obtained from Fischer Scientific India with degree of hydrolysis of 85–89 cS and viscosity of 35–50 cSt. Ferric nitrate was obtained from NICE chemicals, Kerala, India. Since reagents and chemicals were of analytical grade, they were used without purification.

2.2 Synthesis of α-Fe_2O_3 Nanoparticles

Solution combustion synthesis is characterized by highly exothermic redox reactions which yield highly homogeneous products. The starting chemicals used were analytical grade ferric nitrate ($Fe(NO_3)_3\ 9H_2O$) and oxalyl dihydrazide ($C_2H_6N_4O_2$; ODH). The ODH was used as a fuel, which was prepared in the laboratory. An aqueous solution containing stoichiometric amounts of ferric nitrate $Fe(NO_3)_3 9H_2O$ and ODH in 2:1 ratio was taken in a petri dish. Then, the petri dish is introduced into a pre-heated muffle furnace maintained at 300 ± 10 °C. The reaction mixture undergoes thermal dehydration and ignites at one spot with liberation of gaseous products such as oxides of nitrogen and carbon [14, 15]. The combustion propagates throughout the reaction mixture without further need of any external heating, as the heat of the reaction is sufficient for the decomposition of the redox mixture. In low-temperature solution combustion synthesis process, ODH acts as a fuel and it is oxidized by nitrate ions.

2.3 Preparation of PVA/NaCl/ α-Fe_2O_3 Nanocomposites

PVA/NaCl/α-Fe_2O_3 nanocomposites were prepared by solution casting method. PVA was dissolved in distilled water by heating at 60 °C for 16 h under stirring (25 g in 500 ml). This was used as stock solution, 0 wt%. The blends with varying amounts, viz., 20, 40, and 60 wt% (1, 2, and 3 g in 100 ml), of NaCl in stock solution and 2, 4, and 6 wt% (0.1, 0.2, and 0.3 g in 100 ml) of α-Fe_2O_3 nanoparticles in the stock solution were prepared by stirring the composition of the blends for 30 min. The PVA/α-Fe_2O_3/NaCl blend solution was casted onto a cleaned glass plate and dried at room temperature.

2.4 XRD studies

X-ray diffraction patterns were recorded on Rigaku Miniflex II Diffractometer with Ni filtered, CuKα radiation of wavelength 1.542 Å, and a graphite monochromator. The scattered beam from the sample was focused on to a detector. The specifications used for the recording were 30 kV and 15 mA. The sample was scanned in the 2θ range of 6° to 60° with a scanning step of 0.02°.

2.5 FTIR Measurements

The Fourier transformation infrared spectroscopic measurements were performed on Perkin Elmer version 10.03.09 Fourier transform infrared (FTIR) instrument with a resolution of 4 cm^{-1} over the spectral range of 4000–400 cm^{-1} in absorbance mode.

2.6 Scanning Electron Microscopy

The surface morphology of the prepared nanocomposite films was studied by scanning electron microscopy. The scanning electron microscopy (SEM) of blend films with different weight percentages were recorded by Hitachi Scanning Electron Microscope SU3500, Japan, at 15 kV.

2.7 Transmission Electron Microscopy

TEM measurements were done using a Philips transmission electron microscope, model CM200S with operating voltage of 20–200 kV and resolution of 2.4 A°

2.8 VSM

Magnetic measurements were done using a vibrating sample magnetometer at room temperature using Lakeshore Vibrating Sample Magnetometer (VSM) Model 7410.

2.9 Positron Annihilation Lifetime Measurements

The positron lifetime spectrometer with fast-fast coincidence system consisting of BaF_2 scintillators of conical shape connected to photomultiplier tubes of type XP2020/Q with quartz window as detectors was used to document the positron lifetime spectra of polymer nanocomposites. The two similar pieces of the specimen were placed on both sides of a 15 μCi-^{22}Na positron source, deposited on a pure Kapton foil of 0.0127-mm thickness [16]. This sample-source sandwich was placed between the two detectors of PLT to acquire lifetime spectrum. All lifetime measurements were performed at room temperature ,and two to three positron lifetime spectra with more than a million counts under each spectrum were recorded in a time of 2–4 h. Consistently, reproducible spectra were analyzed into three lifetime components with the help of the computer program PATFIT-88 [16], with proper source and background corrections. Source correction term and resolution function were estimated from the lifetime of well-annealed aluminum using the program RESOLUTION [16–18].

3 Theory

3.1 X-Ray Diffraction Data Analysis

For the computation of line profile analysis, the mathematical equations and its elucidations are reproduced due to ephemerality. Bragg reflection profile with the dispensation of crystallite size, lattice strain, and stacking faults can be expressed as [19–21]

$$I_{hkl}(s_{hkl}) = \int_{-\infty}^{\infty} T^{IP}(nd) e^{[2\pi i\zeta(nd)]} e^{[2\pi i\varphi(nd)]} e^{[2\pi i n d s_{hkl}]} d(nd) \tag{1}$$

where $I_{hkl}(s_{hkl})$ is the intensity of a profile in the direction joining the origin to the center of the reflection, T^{IP} is the Fourier transform of instrument profile, $e^{[2\pi i\zeta(nd)]}$ is the average phase factor due to lattice distortion (ζ), and $e^{[2\pi i\varphi(nd)]}$ is due to crystallite size/stacking faults(φ). $L = nd$ (with $d = d_{hkl}$) is the column length. Representing Eq. (1) in the form of Fourier series [22]

$$I_{hkl}(s_{hkl}) = \sum_{n=-\infty}^{\infty} A_{hkl}(n) \cos\{2\pi i n d_{hkl}(s - s_0)\} \tag{2}$$

where $A_{hkl}(n)$ is the corrected Fourier coefficients with Fourier coefficients of instrumental profile function $T^{IP}(nd)$, s is $\sin\theta/\lambda$, and s_0 is the value of s at the peak of the reflection. The average number of unit cells counted in a direction perpendicular to the Bragg plane (hkl) with a notation $<N>$ is referred to as crystallite size, and the crystallite size in angstrom is given by $D_{hkl} = <N> d_{hkl}$ (d_{hkl} is the perpendicular spacing of the (hkl) planes from their origin). The Fourier coefficients $A_{hkl}(n)$ which are functions of the disorder of the

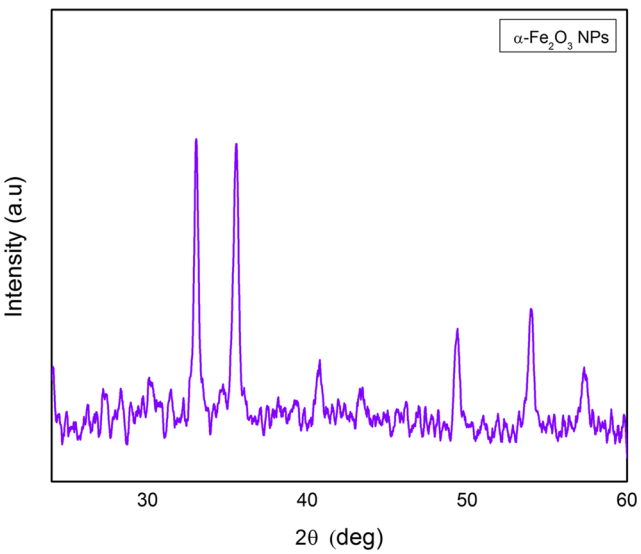

Fig. 1 XRD pattern of α-Fe_2O_3 nanoparticles

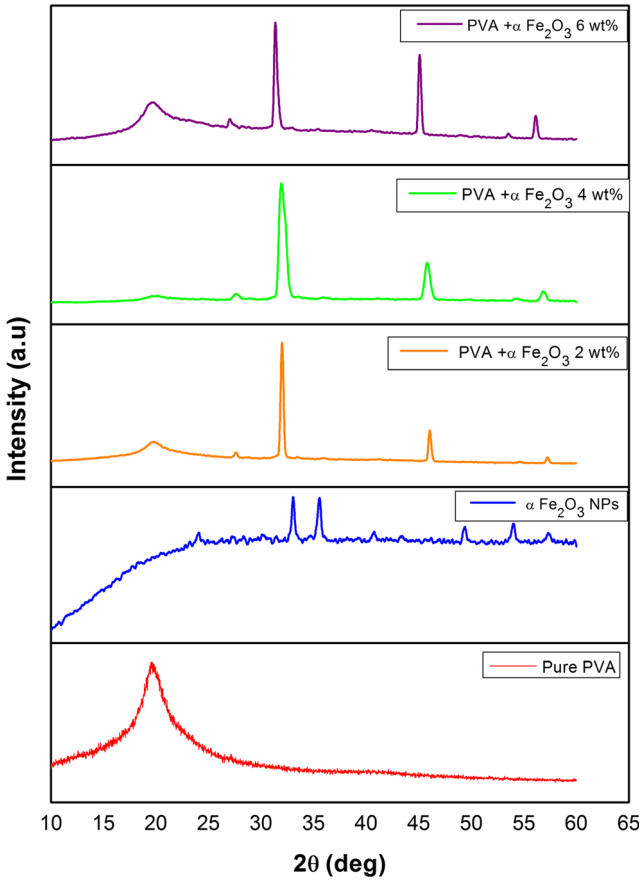

Fig. 2 XRD pattern of Pure PVA and PVA/NaCl/α-Fe_2O_3 nanocomposites

lattice, stacking fault coefficients, and the size of the crystallite can be written as

$$A_{hkl}(n) = A^{s}{}_{hkl}(n).A^{d}{}_{hkl}(n).A^{F}{}_{hkl}(n) \tag{3}$$

Experimental limitation of Fourier analysis of a Bragg reflection profile is addressed by performing the analysis with the introduction of truncated correction [23, 24]. For a paracrystalline material, with Gaussian strain distribution, $A^{d}{}_{hkl}(n)$ can be expressed as [23–25]

$$A^{d}{}_{hkl}(n) = \exp\left(-2\,\pi^2 n^2 m\, g^2\right) \tag{4}$$

where m is the order of the reflection and $g=(\Delta d/d)$ is the lattice strain. Usually, one also defines mean square strain $<\varepsilon^2>$ that is given by g^2/n. This mean square strain is dependent on n (or column length $L=nd$), whereas g is not. Using exponential distribution function for column length [26]

$$A^{S}_{hkl}(n) = \begin{cases} A \quad (0) \quad (1-n/\langle N\rangle) \quad , & ;\text{if } n < p \\ A(0)\{\exp[-\alpha(n-p)]\}/(\alpha N) & ;\text{if } n \geq p \end{cases} \tag{5}$$

where $\alpha = 1/(N-p)$ refers to the width of the distribution and p is the smallest number of unit cells in a column.

According to Warren [23] asymmetry, shift and broadening of the profile correspond to the deformation and twin faults. The sequence of stacking layers is usually denoted by A, B, and C. The right sequence is ABCABC or CBACBA. A stacking fault can be represented by ABCBCABC. A twin fault sequence is ABCABCBACBA. Veltrop [27] has obtained an equation for Fourier coefficients $A^{F}{}_{hkl}(n)$ in terms of the deformation fault (α^d) and twin fault (β) probabilities as

$$A^{F}_{hkl}(n) = \left[1-3\alpha^{d}-2\beta+3\left(\alpha^{d}\right)^2\right]^{\left|(1/2)nd_{hkls}\left(L_0/h_o^2\right)\sigma_{L_0}\right|} \tag{6}$$

where α^d and β are, respectively, the deformation and twin fault probabilities, $L_0=h+k+l$, $h^2{}_0=h^2+k^2+l^2$, and σ_{L_0} is the volume of crystallite with specified L_0. The chance of finding a stacking fault between any two adjacent layers causing a Bragg reflection is denoted by α^d. Generally, α^d is expressed in percentage and the average number of Bragg planes between stacking faults is given by $1/\alpha^d$. The prospect of finding a twin fault between any two adjacent (hkl) layers is defined as the twin fault probability, and the average number of (hkl) layers between twin faults is $1/\beta$. We have reckoned σ_{L_0} to be positive

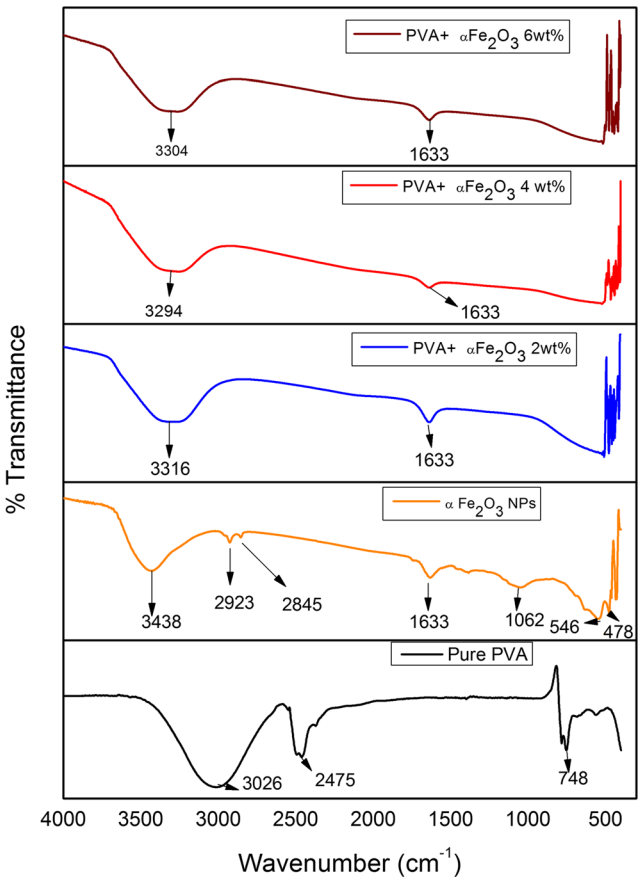

Fig. 3 FTIR spectra of polymer nanocomposites with various weight percentages of salt and nanoparticles

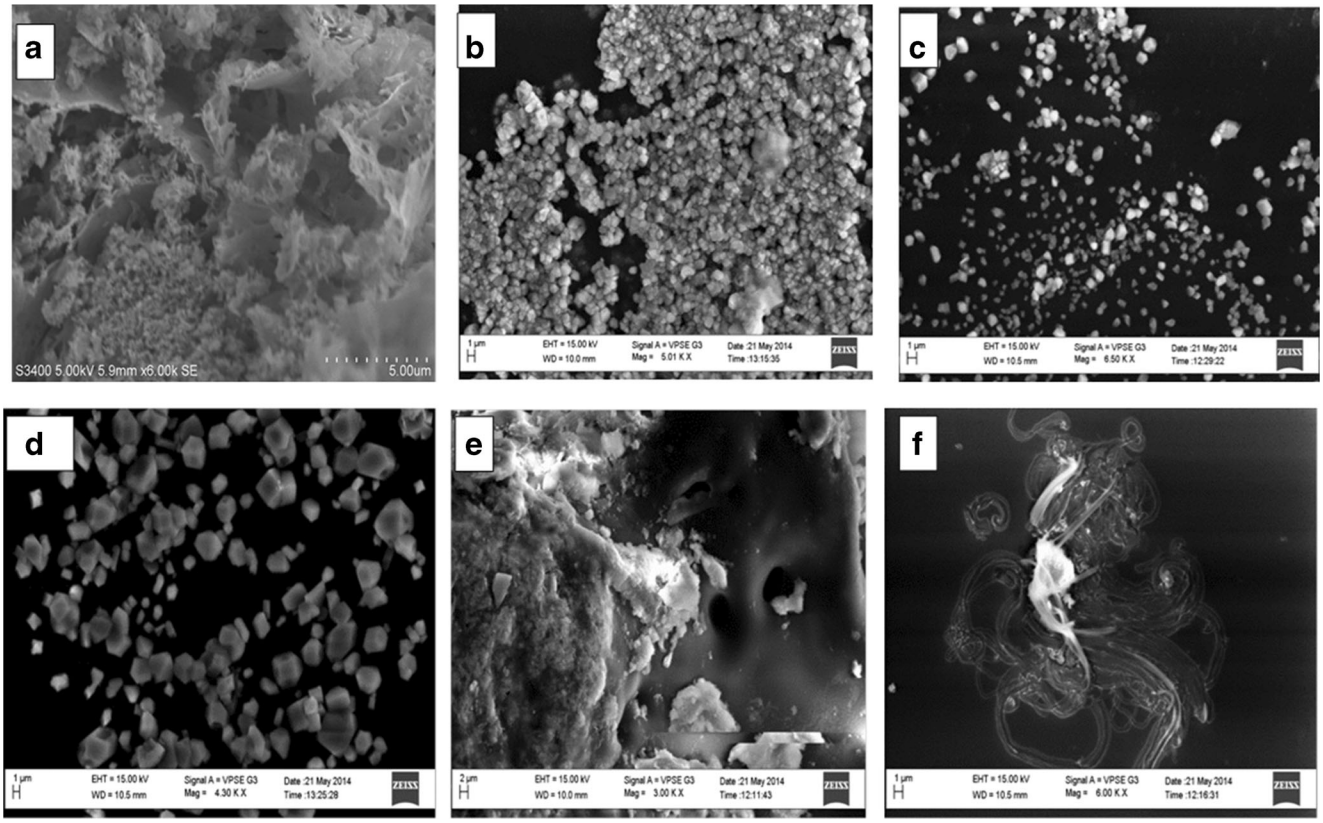

Fig. 4 SEM images of as-prepared α-Fe_2O_3 nanoparticles and of the PVA blended with α-Fe_2O_3 nanoparticles and NaCl with various weight percentages. **a** As-prepared α-Fe_2O_3 nanoparticles; **b** 2 wt%; **c** 4 wt%; **d**, **e** & **f** different magnification

for all reflections (for $L_0 = 3N + 1$ and $N = 0, \pm1, \pm2, \ldots$) studied here. The whole powder pattern of samples was simulated using individual Bragg reflections represented by the above equations using

$$I(s) = \sum_{hkl} (\omega_{hkl} I_{hkl} - BG) \tag{7}$$

where ω_{hkl} is the appropriate weight functions for the (hkl) Bragg reflection. Here s takes the whole range ($2\theta \approx 6°$ to 60°) of X-ray diffraction recording of the sample. BG is an error parameter introduced to correct the background estimations.

3.2 PALS

Based on the theoretical model for molecular liquids [28], free volume hole size is related to o-Ps lifetime (τ_3) represented by Eq. (8) [29]. In this model, positronium is assumed to be

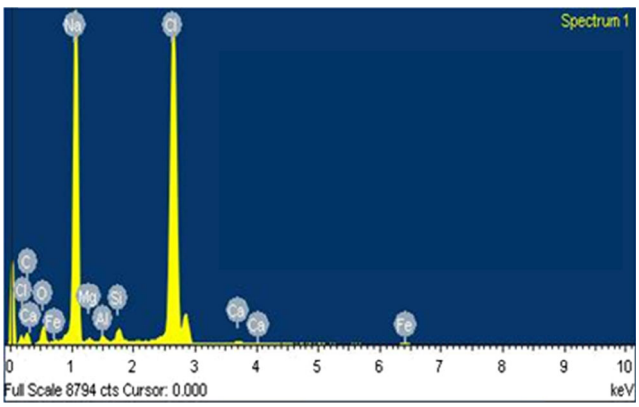

Fig. 5 EDAX spectrum of the PVA/NaCl/α-Fe_2O_3 nanocomposites

Table 1 EDAX elemental microanalysis of the PVA/Fe_2O_3 nanocomposites

Element	Weight %	Atomic %
C K	18.40	34.09
O K	6.86	9.54
Na K	27.47	26.59
Mg K	0.27	0.25
Al K	0.45	0.37
Si K	1.18	0.94
Cl K	43.87	27.55
Ca K	0.46	0.26
Fe K	1.03	0.41
Total	100	

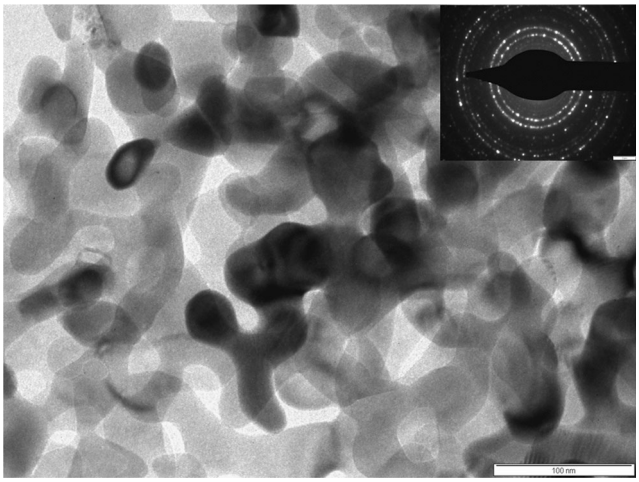

Fig. 6 TEM image of the α-Fe_2O_3 nanoparticles with the inset SAED pattern

localized in a spherical potential well having an infinite potential barrier of radius R_0 with an electron layer in the region

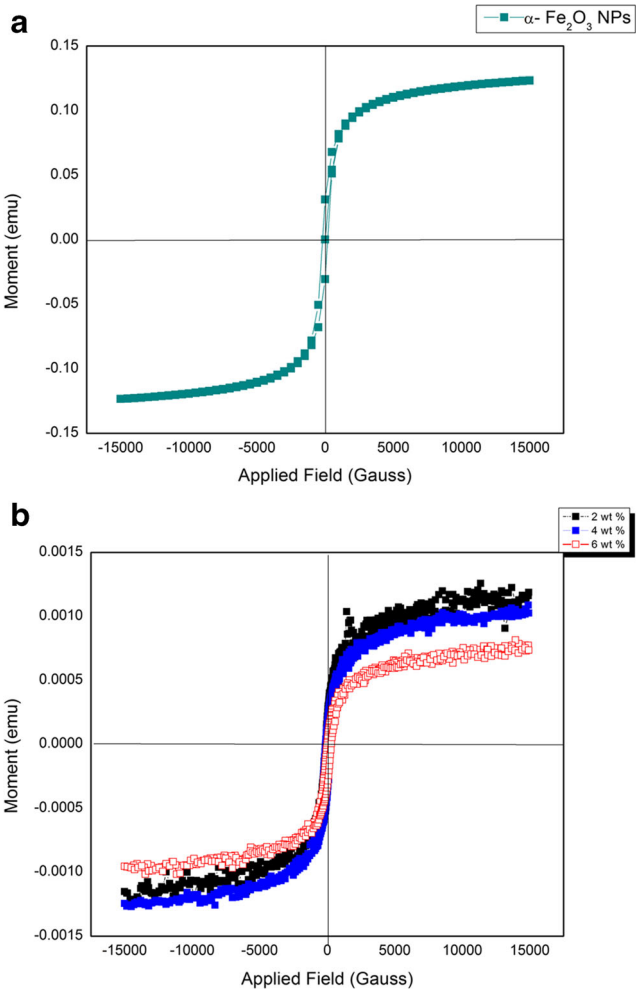

Fig. 7 **a** Magnetization versus applied field curve for α-Fe_2O_3 nanoparticles at 300 K. **b** Magnetization versus applied field curve for PVA/NaCl/α-Fe_2O_3 nanocomposites at 300 K

$R<r<R_0$. The semblance between τ_3 and the radius R of the free volume hole or cavity is

$$\lambda = \frac{1}{\tau_3} = 2P = 2\left[1 - \left(\frac{R}{R_0}\right) + \left(\frac{1}{2\pi}\right)\mathrm{Sin}\left(\frac{2\pi R}{R_0}\right)\right] ns^{-1} \quad (8)$$

where $R_0 = R + \delta R$ and δR is an adjustable parameter.

By fitting Eq. (8) with τ_3 values for known hole sizes in porous materials like zeolites, a value of $\delta R = 0.1657$ nm was obtained. With this value of δR, the free volume radius R has been calculated from Eq. (8) and the average size of the free volume holes (V_f) is evaluated as

$$V_f = (4/3)\,\pi\,R^3 \quad (9)$$

The fractional free volume or the free volume content (F_v) can then be estimated as

$$F_v = C\,V_f I_3 \quad (10)$$

where C is structural constant, 0.0018 $Å^3$ [30], V_f is the free volume hole size, and I_3 is the o-Ps intensity as suggested in the literature [30–32].

4 Results and Discussion

4.1 X-Ray Diffraction

Figure 1 shows the powder X-ray diffraction pattern of as-prepared α-Fe_2O_3 sample at room temperature. The four strongest X-ray diffraction (XRD) peaks were detected corresponding to Bragg angles 33.01°, 35.53°, 49.34°, and 54.04°, respectively. All the diffraction peaks were readily indexed to a pure rhombohedral phase [space group: R-3c (167)] of α-Fe_2O_3 (JCPDS card No. 72–469) with $a = 5.038$ Å and $c = 13.772$ Å. The diffracted patterns are well matched with the literature. No impurity peaks were observed. The crystallite size was calculated by Scherrer's formula and is found to be approximately 15–20 nm. The XRD patterns of the prepared composite films (Fig. 2) indicate the shifting of the XRD peaks, toward the lower angles demonstrating the intercalated structure [33–35] due to the presence of nanocomposites

4.2 FTIR Spectroscopy

FTIR spectra of pristine PVA and prepared magnetic nanocomposites are shown in Fig. 3. The spectra indicate absorption bands of Fe–O at 546, 460,429, and 437 cm^{-1} [36, 37]. However, the FTIR spectrum shows these characteristic peaks of Fe–O; also, in addition to these peaks, new peaks also appear for the nanocomposites. This result confirms the presence of α-Fe_2O_3nanoparticles in the prepared nanocomposites [38]. The spectra shows a strong broad absorption band at

Table 2 Microstructural parameters and stacking faults for PVA-doped Fe_2O_3 using exponential distribution function

Samples	Peaks	2θ (deg)	α	*g* (%)	d_{hkl} (Å)	<*N*>	D_s (Å)	α^d	β	delta (E-03)	Crystallite area (Å^2)
PVA	1	19.7	2.302	0.5	4.502	7.5	33.7	3.38E-7	7.21E-5	3.04	1000
	2	41.91	3.413	0.5	2.153	13.8	29.7	3.10E-5	8.54E-5		
PVA + Fe_2O_3 (2 wt%)	1	19.86	4.038	0	4.466	8.45	37.73	3.07E-5	4.53E-6	0.616	13465
	2	27.6	0.350	0	3.229	66.48	214.6	3.43E-6	3.77E-6		
	3	31.99	1.679	0.5	2.795	105	293.4	4.26E-6	9.90E-6		
	4	46.03	0.870	0	1.970	181.2	356.9	2.21E-6	1.94E-6		
PVA + Fe_2O_3 (4 wt%)	1	19.92	1.968	0	4.453	13.40	59.67	1.18E-5	1.23E-5	0.878	11546
	2	27.63	2.275	0	3.225	60	193.5	1.21E-5	3.43E-5		
	3	31.97	2.285	0	2.797	65	181.8	2.23E-5	3.62E-5		
	4	45.80	5.532	0.5	1.979	83	164.2	1.68E-5	1.18E-5		
PVA + Fe_2O_3 (6 wt%)	1	19.66	0.705	0	4.511	7.10	32.02	2.08E-7	1.76E-5	1.40	10041
	2	27.02	2.890	0	3.297	50	164.8	8.00E-6	5.98E-5		
	3	31.35	1.713	0	2.851	110	313.6	8.65E-6	1.06E-5		
	4	45.08	0.065	0	2.009	154	309.3	1.40E-6	1.55E-6		

The quantified microstructural parameters: <*N*>, crystallite size; D_s, crystallite size; *g*, lattice strain; α, width of the distribution; α^d, stacking faults; β, twin faults

~3300 cm^{-1} which is assigned to O–H stretching vibration of PVA. The band corresponding to C–H asymmetric stretching vibration occurred at 2475 cm^{-1} [39]. Furthermore, for PVA nanocomposites with α-Fe_2O_3 nanoparticles, the bands at 3316, 3294, and 3304 cm^{-1} and as shown in the spectrum have shifted to higher wave number compared to the characteristic bands of pristine PVA, and the absorption bands at 2923 and 2845 cm^{-1} of α-Fe_2O_3 nanoparticles disappear, indicating the interaction between nanoparticles and the polymer matrix [38, 39].

4.3 SEM

The SEM images as shown in Fig. 4a exhibit non-spherical, flake-like agglomerated particle morphology for Fe_2O_3 nanoparticles. The SEM micrographs of nanocomposites of 2, 4, and 6 wt% are shown in Fig. 4b, c, d. As seen in these images (b) and (d), α-Fe_2O_3 nanoparticles are uniformly distributed whereas (c) shows a distorted distribution of nanoparticles.

4.4 EDAX

Figure 5 shows the energy-dispersive analysis by X-ray (EDAX) of the nanocomposite films. The respective weight percentages of NaCl and metal are shown in Table 1. The formation of nanocomposites is confirmed by the presence of Iron (Fe) in the EDAX spectrum which supplements the XRD and FTIR results.

4.5 TEM

The TEM images of the synthesized α-Fe_2O_3 nanoparticles as shown in Fig. 6 via solution combustion method show that the particles obtained are non-spherical and dumbbell-shaped. The average size of the nanoparticles are about 20–25 nm which is in good agreement with the XRD results. The corresponding SAED pattern (Fig. 6 inset) of the α-Fe_2O_3 nanoparticles shows the clear diffraction spots with concentric rings indicating the polycrystallinity of the nanoparticles.

4.6 VSM

The magnetic measurements show the coercevity of the α-Fe_2O_3 nanoparticles to be 188.9 G and retentivity to be equal to 30.843E-3 as shown in Fig. 7a. From Fig. 7b, the coercevity for the nanocomposites for 2, 4, and 6 wt% was found to be 130.89, 197.8, and 168.57 G, respectively, and the retentivity of the nanocomposites was found to be 210.8E-6, 605.8E-6, and 400.60E-6, respectively. Also, the saturation magnetization values of nanocomposites were found to be less than those of the synthesized α-Fe_2O_3 nanoparticles. This reduction in saturation magnetization values and retentivity of nanocomposite films which are much lower than those of the synthesized nanoparticles could be attributed to the superparamagnetic nature of polymer matrix [40–42].

4.7 Whole-Pattern Fitting

The computed values of crystallite size <*N*>, lattice strain (*g* in %), stacking fault probability, and twin fault probability are given in Table 2 for pure PVA and PVA/Fe_2O_3 nanocomposites using exponential column length distribution. The observed variation in the microstructural parameters given in Table 2 is due to a twofold refinement [43]. First, we have carried out the line profile analysis of the extracted profiles from overlapping regions, which is a standard procedure to

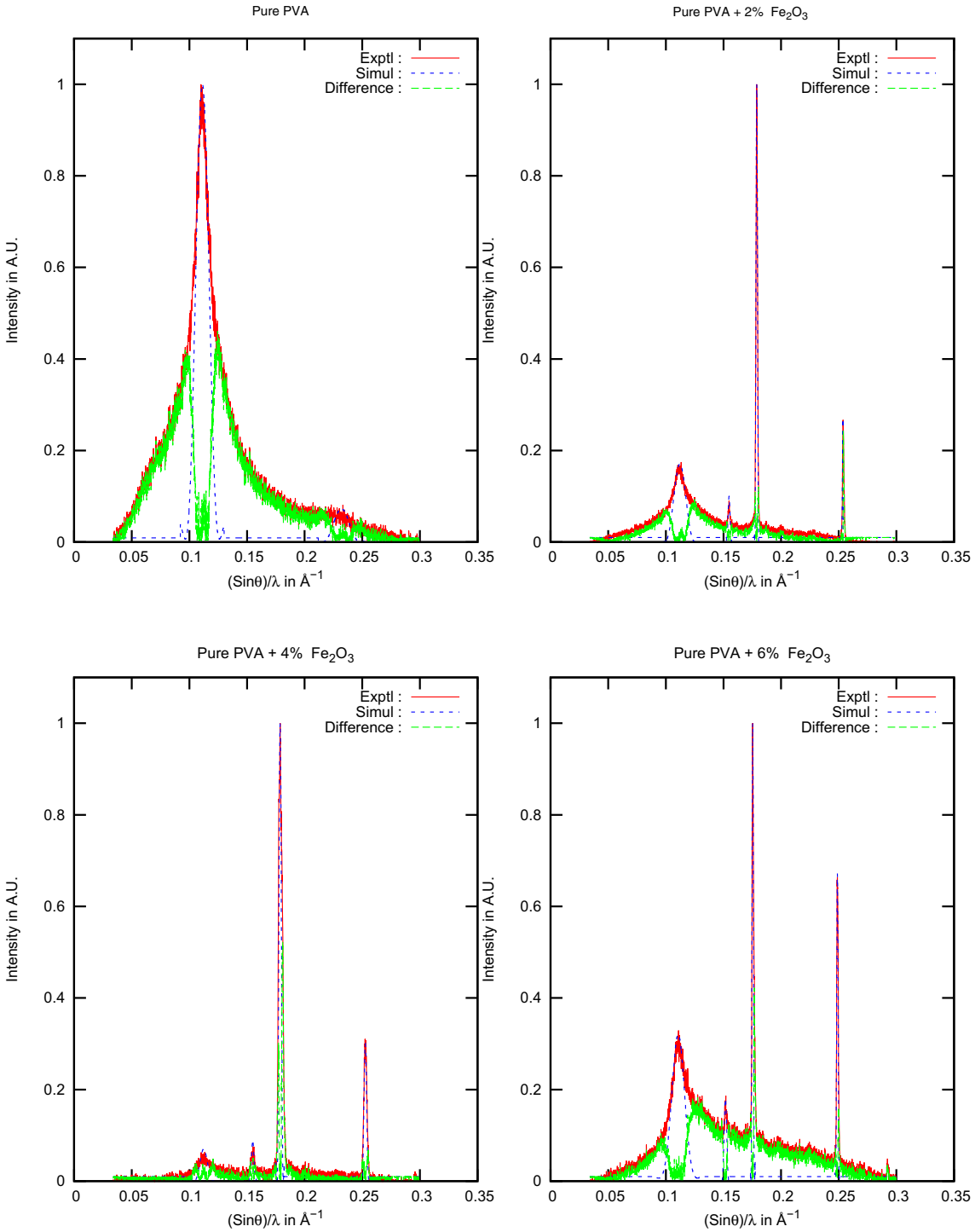

Fig. 8 Whole powder pattern for pure PVA and PVA/NaCl/α-Fe_2O_3 nanocomposites

compute the microstructural parameters. Second, the range of overlapping regions determines the extent of broadening of the reflections. In fact, the broadening may decrease if the reflections are closer together and hence results in an increase in the crystallite size values. It is well known that the Fourier method gives a reliable set of microstructural parameters, and we have shown that in addition to these values, one can also compute reliable fault probabilities which are found to decrease in nanocomposites compared to pure PVA. We observe that the lattice strain in 2 and 4 wt% is 0.5 % and average crystallite area decreases from 13,465 to 10,041 $Å^2$ as the nanoparticle loading increases in the nanocomposites. Figure 8 shows simulated and experimental profiles for nanocomposites of 2, 4, and 6 wt% obtained with exponential

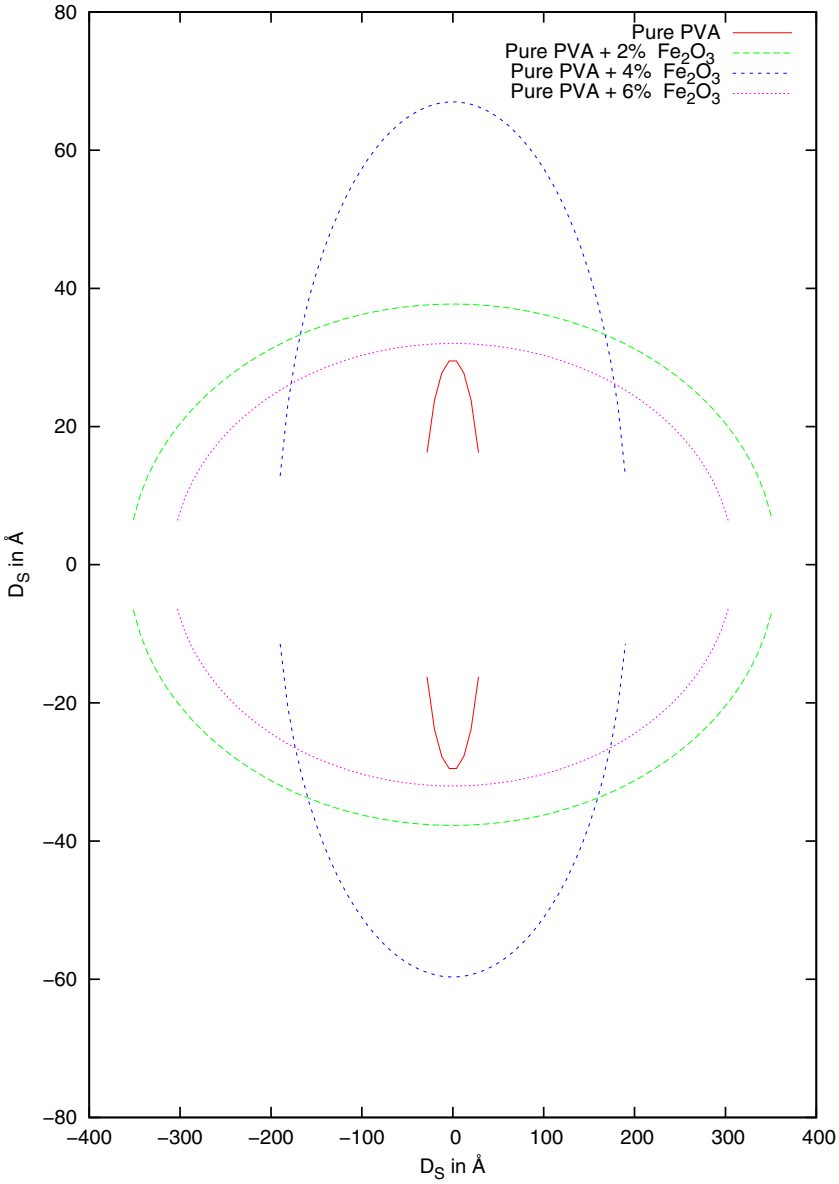

Fig. 9 Variation of crystallite shape ellipsoid for pure PVA and PVA/NaCl/α-Fe_2O_3 nanocomposites

column length distribution. A graphical plot of the crystallite shape ellipsoid was obtained by projecting the results into a plane and is given in Fig. 9. The experimental and simulated profiles for nanocomposite films of different weight percentages are shown in Fig. 8, with the fitting of the profiles being good using whole pattern ($2\theta \approx 6°$ to 60°). The refinement was carried out using the computed microstructural parameters in which the twin faults and stacking faults did not vary much and statistical deviation was less than 5 %.

4.8 Positron Lifetime Spectroscopy

PALS measurements revealed that the free volume properties are strongly affected by the amount and type of filler; the free volume size dramatically increases by increasing the filler content [17, 18]. Since we are interested in free volume hole size and their concentration in polyvinyl alcohol (PVA), only the third and long lifetime component, viz., o-Ps lifetime (τ_3), and o-Ps intensity derived from the PATFIT program are reported here. Figure 10a, b, c shows the plots of o-Ps lifetime (τ_3), o-Ps intensity (I_3), free volume (V_f), and relative fractional free volume as a function of nanoparticle concentration, respectively. The values of o-Ps lifetime (τ_3) and its intensity (I_3) for as received PVA sample are 1.50 ns and 11.78 %, respectively, as given in Table 3. From Fig. 1a, it is observed that the o-Ps lifetime (τ_3) increases gradually as a function of nanoparticle concentration and we can observe about 219 ps increase from1.50 ns to1.71 ns at 6 wt% of nanocomposites. This indicates the increase of free volume hole size (V_f) from 54.47 to 72.18 $Å^3$ at 6 wt% of nanocomposites. This increase in free volume hole size (V_f) can be explained as follows. In amorphous polymers, the o-Ps is preferentially formed and

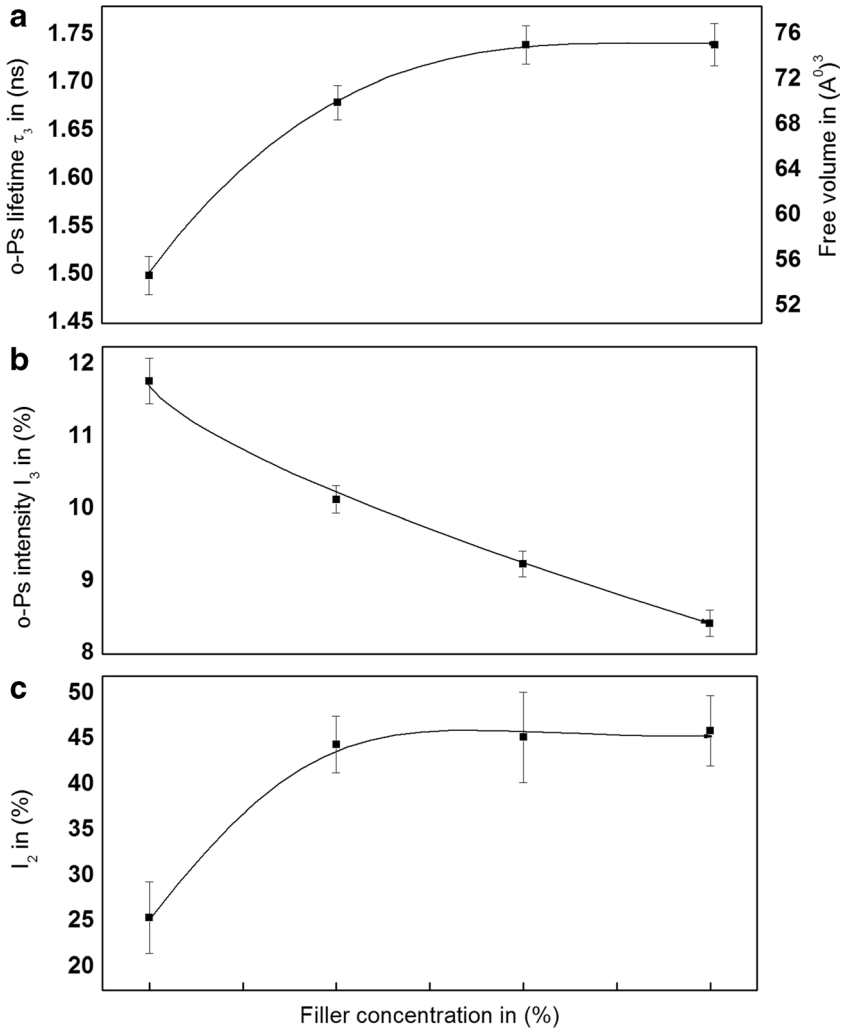

Fig. 10 Plots of **a** o-Ps lifetime (τ_3) and free volume (V_f), **b** o-Ps intensity (I_3), **c** relative fractional free volume as a function of nanoparticle concentration, respectively

localized within the free volume holes. However, in the semi-crystalline polymers, o-Ps may be formed with in the interfacial free volumes, at vacancy type defects at the crystalline amorphous interface region [44, 45] and polymer-inorganic particles interface [46]. PALS parameters are average values taking into account the different dimensions of holes related to the phases and interfaces present in the materials, the increase of free volume size in the PVA nanocomposite is attributed to the formation of interface between PVA and Fe_2O_3 nanoparticles which is augmented by the FTIR results.

The variation of o-Ps intensity (I_3) and positrons annihilating at the crystalline amorphous interface (I_2) as a function of nanoparticle concentration is as shown in Fig. 10b, c, respectively. The intensity of o-Ps annihilation (I_3) correlates with the amount of the free volume or the number of voids in the sample [18]. From Fig. 10b, around 3.35 % of reduction in I_3 value at 6 wt% of nanocomposites as compared to the as-received PVA sample can be observed. This may be due to the inhibition of o-Ps formation by providing an additional positron interaction mechanism, which restricts with positronium (Ps) formation in the polymer [18]. The intensity of positron annihilation (I_2) at the interface increases as a function of nanoparticle concentration. This increase is attributed to the formation of an interfacial layer of nanoparticles with PVA and due to the strong interaction between nanoparticles and PVA matrix [29–31].

Table 3 Orthopositronium lifetime results in PVA magnetic nanocomposites

Sample	τ_3 (ns)	I_3 (%)	I_2 (%)	V_f (Å^3)
PVA (0 wt%)	1.5000 ± 0.0200	11.78 ± 0.31	25.48 ± 3.93	54.47 ± 1.28
PVA + Fe_2O_3 (2 wt%)	1.6807 ± 0.0184	10.14 ± 0.19	44.49 ± 3.10	68.88 ± 1.30
PVA + Fe_2O_3 (4 wt%)	1.7476 ± 0.0207	09.25 ± 0.18	45.28 ± 4.97	74.64 ± 1.53
PVA + Fe_2O_3 (6 wt%)	1.7414 ± 0.0207	08.43 ± 0.18	46.00 ± 3.87	74.13 ± 1.56

5 Conclusions

(a) We have reported the microstructural studies of PVA/Fe_2O_3 nanocomposites of different weight percentages by whole-pattern fitting technique and positron annihilation lifetime spectroscopy.
(b) From the VSM data, we observe that the prepared nanocomposites exhibit magnetic property.
(c) The evaluated microstructural parameters such as stacking fault and twin fault probabilities obtained by Fourier coefficient method indicate that the values are low, because there are too many layers between two successive deformation fault layers.
(d) The stacking faults and twin faults vary with nanoparticle concentration.
(e) An increase of o-Ps lifetime (τ_3) and free volume size was observed as a function of nanoparticle concentration.
(f) The intensity of o-Ps annihilation (I_3) decreases and the intensity of positron annihilation (I_2) increases with the nanoparticle loading which can be attributed to the interfacial surface interactions between nanoparticles and the polymer matrix.
(g) Ferric ions inhibit the o-Ps formation in polyvinyl alcohol, which is indicated by the decreased value of o-Ps intensity in nanocomposites, and increased I_2 value indicates the increased annihilation rate at the interface region.

Acknowledgments The authors thank the Department of Chemistry, MSRIT, Bangalore, and Department of Physics, University of Mysore, for providing the laboratory facilities, SAIF IITB, SAIF IITM, CIF-IITG, SAIF Kochi, and PPISR –Bangalore for Characterization of the samples

References

1. M.M. Aparna, B. Soumya, M. Dipankar, S. Arvind, N. Suprabha, J. Mater. Sci. Mater. Med. **21**, 2365 (2010)
2. N. Bock, A. Riminucci, C. Dionigi, A. Russo, A. Tampieri, E. Landi, V.A. Goranov, M. Marcacci, V. Dediu, Acta Biomater. **6**, 786 (2010)
3. B. Amir, A. Ahmad, J. Appl. Polym. Sci. (2015). doi:10.1002/app.41969
4. G. Zhanhu, P. Tony, C. Oyoung, W. Ying, H. Thomas, J. Mater. Chem. **16**, 2800 (2006)
5. Š. Monika, S.M. Gražyna, B. Karla, Sci. Adv. Mater. **3**, 1 (2011)
6. K. Susheel, K. Sarita, K. Amit, H. Yuvaraj, K. Bandna, R. Kumar, Colloid Polym. Sci. **292**, 2025 (2014)
7. A.L. Lin, H. Peng, Z. Liu, T. Wu, C. Su, K.P. Loh, Ariando, W. Chen, A.T.S. Wee, Small **10**, 1945 (2014)
8. L.F. Gamarra, L.F. Pavon, L. CMarti, W.M. Pontuschka, J.B. Mamani, A.J. Costa-Filho, E.D. Vieira, C.A. Moreira-Filho, E. Amaro Jr., J. Phys. Condens. Matter **20**, 204150 (2008)
9. T.A.P. Rocha-Santos, TrAC Trends Anal. Chem. **62**, 28 (2014)
10. H. Tina, M. Majid, J. Mater. Chem. B. **2**, 272 (2014)
11. S. Parveen, C. Veena, N. Vijayan, R.K. Kotnala, J. Phys. Chem. C. **116**, 13403 (2012)
12. K.V. Aneeshkumar, H.B. Ravikumar, C. Ranganathaiah, J. Appl. Polym. Sci. **130**, 793 (2013)
13. H.B. Ravikumar, C. Ranganathaiah, G.N. Kumaraswamy, S. Thomas, Polymer **46**, 2372 (2005)
14. K.C. Patil, M.S. Hegde, T. Rattan, S.T. Aruna, *Chemistry of Nanocrystalline Oxide Materials, Combustion synthesis, Properties and Applications* (World Scientific Publishing, UK, 2008), pp. 42–45
15. A.A. Jahagirdar, N. Dhananjaya, D.L. Monika, C.R. Kesavulu, H. Nagabhushana, S.C. Sharma, B.M. Nagabhushana, C. Shivakumara, J.L. Rao, R.P.S. Chakradhar, Spectrochim. Acta A Mol. Biomol. Spectrosc. **104**, 512 (2013)
16. P. Kirkegaard, N.J. Pedersen, M. Eldrup, *Riso Nat Lab Reports* (Denmark, M-2740, 1989)
17. E.H.A. Aly, J. Appl. Sci. **8**, 147 (2011)
18. S. Awad, H. Chen, Guodong, Macromolecules **44**, 29 (2011)
19. A.R. Niranjana, S. Divakara, R.S. Somshekar, Indian J. Fibre Text. Res. **36**, 9 (2011)
20. S.S. Mahesh, M.B. NandaPrakash, R. Somashekar, World Res. J. Appl. Phys. **4**, 54 (2013)
21. S.S. Mahesh, K.S. Prashanth, S. Ananda, M.B. Nanda Prakash, R. Somashekar, Int. J. Innov. Res. Sci. Eng. **1**, 5 (2013)
22. P. Scardi, M. Leoni, Acta Crystallogr. A **58**, 190 (2002)
23. B.E. Warren, *X – ray Diffraction* (Addision – Wesley, New York, 1969), pp. 105–115
24. R. Somashekar, I.H. Hall, P.D. Carr, J. Appl. Crystallogr. **22**, 363 (1989)
25. B.E. Warren, Prog. Met. Phys. **8**, 147 (1959)
26. B.E. Warren, B.L. Averbach, J. Appl. Phys. **21**, 595 (1950)
27. L. Veltrop, R. Delhez, Th.H. De Keijser, E.J. Mittemeijer, D.J. Reefman, J. Appl. Crystallogr. **33**, 296 (2000)
28. M. Eldrup, D. Lightbody, J.N. Sherwood, Chem. Phys. **63**, 51 (1981)
29. H. Nakanishi, S.J. Wang, Y.C. Jean, Proceedings of International Symposium on Positron Annihilation Studies in Fluids, S.C. Sharma, editor, World Scientific, Singapore (1988)
30. Y.C. Jean, Positron annihilation spectroscopy for chemical analysis: a novel probe for microstructural analysis of polymers. Microchem. J. **42**, 72 (1990)
31. V. Ravindrachary, Ismayil, P.N. Suresh, D. Dhanadeep, P.K. Pujari, Polym. Degrad. Stab. **96**, 1676 (2011)
32. Ismayil, V. Ravindrachary, R.F. Bhajantri, S.D. Praveena, B. Poojary, D. Dhanadeep, P.K. Pujari, Polym. Degrad. Stab. **95**, 1083 (2010)
33. R.S. Sinha, M. Bousmina, Prog. Mater. Sci. **50**, 962 (2005)
34. R.K.G. Naderi, G.R. Bakhshandeh, M.H.R. Ghoreishy, Iran. Polym. J. **20**, 41 (2011)
35. M. Alexandre, P. Dubois, Mater. Sci. Eng. **28**, 1 (2000)
36. A.B. Ruhul, B. Palash, K.D. Birinchi, J. Saudi, Chem. Soc. (2014). doi:10.1016/j.jscs.2013.12.010
37. A.A. Jahagirdar, M.N. Zulfiqar Ahmed, N. Donappa, H. Nagabhushana, B.M. Nagabhushana, Trans. Indian Ceram. Soc. **70**, 159 (2011)
38. H.H.A. Samer, E.E.Z. Mohamed, U.K. Aminu, G. Benjamin, F. Sharida, J.W. Thomas, Z.H. Mohd, BioMed. Res. Int. **2014**, 651831 (2014)
39. H.N. Chandrakala, B. Ramaraj, Shivakumaraiah, G.M. Madhu, Siddaramaiah, J. Mater. Sci **47**, 8076 (2012)
40. A. Seyed, G. Barari, E. Hossein, S. Ebrahim, J. Vinyl, Addit. Technol. (2014). doi:10.1002/vnl.21449
41. S. Ahangar, H.N. Sheikh, B.L. Kalsotra, Synth. React. Inorg. Met.-Org. Nano-Metal Chem. **42**, 892 (2012)
42. F.S. Mohammad Doulabi, M. Mohsen-Nia, Iran. Polym. J. **22**, 9 (2013)
43. P.T. Niranjana, S.S. Mahesh, M.B. Nanda Prakash, T. Demappa, R.Somashekar, IJLTEMAS. 3, (2014)
44. M.N. Chandrashekara, C. Ranganathaiah, Colloids Surf. B: Biointerfaces **69**, 129 (2009)
45. M.N. Chandrashekara, C. Ranganathaiah, J. Photochem. Photobiol. B Biol. **101**, 286 (2010)
46. P.E. Mallon, Y.C. Jean, D.M. Schrader, *Principles and applications of positron & positronium chemistry* (World Scientific, Singapore, 2003), pp. 253–277